Inorganic Chemistry

Article

pubs.acs.org/IC

Conservation of Helicity in a Chiral Pyrrol-2-yl Schiff-Base Ligand and Its Transition Metal Complexes

Zahra Dezhahang, Mohammad Reza Poopari, Joseph Cheramy, and Yunjie Xu*

Department of Chemistry, University of Alberta, Edmonton, Alberta T6G 2G2, Canada

Supporting Information

ABSTRACT: Tetradentate enantiopure Schiff-base ligand (*R*,*R*) and (*S*,*S*)-bis(pyrrol-2-ylmethyleneamine)-cyclohexane (H_2L) and its five transition metal complexes with Ni(II), Cu(II), Zn(II), Pd(II), and Pt(II) were synthesized. Their structural properties, in particular, the ligand chirality, coordination topology, and the resulting helicity in solution, were investigated by using IR, vibrational circular dichroism (VCD), UV−vis, and electronic circular dichroism (ECD) spectroscopies, complemented with density functional theory calculations. Conformational searches and the associated spectral simulations for the ligands and the complexes were performed at the B3LYP/Gen level. Comparison of the experimental and theoretical IR and VCD spectral signatures of these complexes reveal that the Zn complex takes on a dinuclear, distorted tetrahedral coordination topology around the metal centers, whereas the other four metal complexes adopt the mononuclear, distorted square-planar coordination arrangement in solution. The helicity of all systems studied was identified to be *M* with the (*R*,*R*) ligand and *P* with the (*S*,*S*) ligand, dictated by the ligand chirality and the strong preference for the chair configuration by the cyclohexane moiety. Furthermore, the resulting helicity was found to dominate the ECD spectral features, even though the helicity-determining angles are close to zero for the nearly square-planar metal complexes. The related VCD spectral features are sensitive to both helicity of the complex and the chirality of the ligands, as well as the coordination topology. The simulated ECD spectra for the *P* and *M* helicity of the $[Zn\text{-}(R,R)\text{-}L]_2$ complex shows almost mirror-imaged ECD spectral features, whereas very similar ECD spectra were recently reported for the *P*- and *M*-dinuclear Mn complexes with a di-μ-oxo dimetal core as a linker. We highlight the advantages of utilizing multiple chiroptical techniques and theoretical spectral simulations to correlate chiroptical spectral features with multiple chirality and helicity elements in the systems.

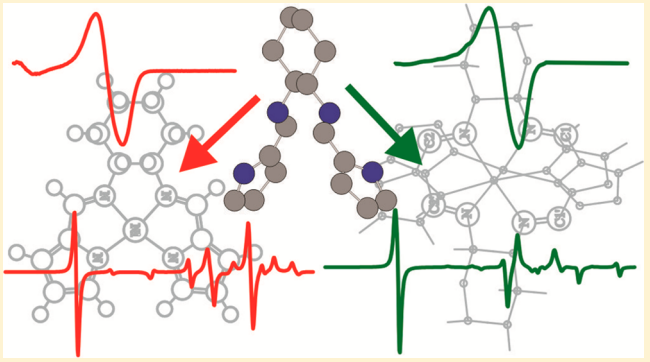

1. INTRODUCTION

Chiral transition metal coordination complexes have attracted substantial research attention because of their wide range of applications in asymmetric catalysis.[1] Studies of transition metal complexes often rely on X-ray crystallography to provide detailed structural information including chirality of the ligands and induced chirality or helicity at the metal centers. On the other hand, researchers have increasingly recognized the dynamic nature of structures in solution. Indeed, these complexes may adopt very different structures in solution compared to those in solid.[2−6] For example, switching to another solvent can modify induced-helicity preference at the metal centers.

In recent years, with the significant advances in both experimental and theoretical vibrational circular dichroism (VCD) spectroscopy and also in theoretical electronic circular dichroism (ECD) spectroscopy, these two chiroptical techniques have seen an increase in their applications in the field of coordination chemistry, especially for transition metal complexes.[7,8] In particular, one can apply these two chiroptical techniques complemented with density functional theory (DFT) calculations to extract structural information in solution, such as conformational distribution and induced helicity of transition metal complexes. A VCD spectrum often contains a substantial number of well-resolved vibrational bands in the fingerprint region. Furthermore, VCD spectral simulations are based on the ground-state electronic structure calculations, which have become quite reliable.[9,10] Both these factors make VCD a powerful tool for coordination chemistry. For example, Sato and co-workers applied VCD spectroscopy to monitor how a chiral Schiff base Ni(II) complex with a binaphthyl moiety transforms reversibly between the square-planar, tetrahedral, and octahedral configurations, depending on solvents and temperature.[6] Conformational changes of chiral binaphthyl diphosphine ligands upon complexation with the Pd(II) ion were revealed by the associated VCD spectral features.[11]

One subject of considerable recent interest is the resulting helicity in these metal complexes or helicates and how factors

Received: February 16, 2015
Published: April 14, 2015

DOI: 10.1021/acs.inorgchem.5b00386
Inorg. Chem. 2015, 54, 4539−4549

such as solvent,[2,3] substitution at ligands,[4,5] and properties of metal centers influence its preference.[12,13] In a recent VCD study, Merten et al. showed that DMSO favors the formation of the Λ-stereoisomer of a tris(diamine)nickel(II) complex and acetonitrile favors the Δ form, whereas in the solid state these two stereoisomers coexist with a ratio of 50:50.2.[2] A number of studies on structures and diastereoselectivity of tetracoordinated transition metal complexes with N,O-chelate Schiff base ligands[14] in solution by VCD and/or ECD spectroscopy have been reported recently.[5,15] These studies demonstrated that the preference for the Δ or Λ form can be quite different in solution and in solid state and such preference can also be switched upon change of solvents. Clearly, relying on the X-ray crystallography alone is not sufficient to determine the induced helicity in solution. This point is especially important considering that such transition metal catalysts are often used in stereoselective syntheses in solution. In addition, these studies highlight the deficiency of the empirical spectral assignment procedure and the importance in applying theoretical modeling to interpret the experimental VCD and ECD spectra to extract solution structural information reliably.

In the present paper, we focus on applying VCD and ECD spectroscopy together with DFT calculations to probe structural properties of a series of chiral transition metal (M = Ni(II), Cu(II), Pd(II), Pt(II), and Zn(II)) complexes with the bis(pyrrol-2-ylmethyleneamine)-cyclohexane ligand (H_2L) directly in solution. The H_2L ligand is of particular interest as there are several examples of similar metal−ligand complexes being used effectively in enantioselective catalysis.[16−19] A new application of this type of metal complex is in self-assembly and building of supramolecules, in particular, supramolecular hetero- and homonuclear helices.[20−23] For example, Setsune and co-workers reported that in single helicates of dipalladium(II) hexapyrroles, introduction of a related ligand, 1-cyclohexylethylamine, to the two terminal formyl groups significantly enhanced diastereoselectivity in favoring one helical isomer.[22] Figure 1 summarizes the five complexes and the ligand investigated in this study. Both the ligand and the complexes were synthesized following previous literature.[21,24,25] We performed both experimental and theoretical IR and VCD studies of all six systems, as well as the related theoretical simulation of UV−vis and ECD spectra. In the following, we demonstrate that the VCD spectral features can be used to identify not only the ligand chirality directly in solution but also the resulting helicity, as well as ligand-to-metal coordination topology, that is, mononuclear versus dinuclear arrangement. In addition, we investigate which key factor, ligand chirality or induced helicity, influences the appearance of ECD spectra of these metal complexes the most and compare the results to a recent study on the di-μ-oxo dimanganese(IV) and dititanium(IV) complexes[12] to shed light on the similarity and difference in the formation of their diastereomeric preference.

2. RESULTS AND DISCUSSION

2.1. Experimental and Theoretical IR, VCD, UV−vis, and ECD Spectra of the Ligand. The (*R*,*R*)-H_2L ligand is similar to another picolylamine-type ligand, *N*,*N*′-bis(pyridine-2-ylmethylene)-(*S*,*S*)-1,2-cyclohexanediamine, which was studied using VCD spectroscopy recently.[26] In the current ligand, the pyridine unit is replaced by a pyrrole functional group. The replacement of pyridine with pyrrole brings substantial rigidity to the structure. The lone electron pairs of the nitrogen atoms are involved in the resonance with the *p*-electrons of the

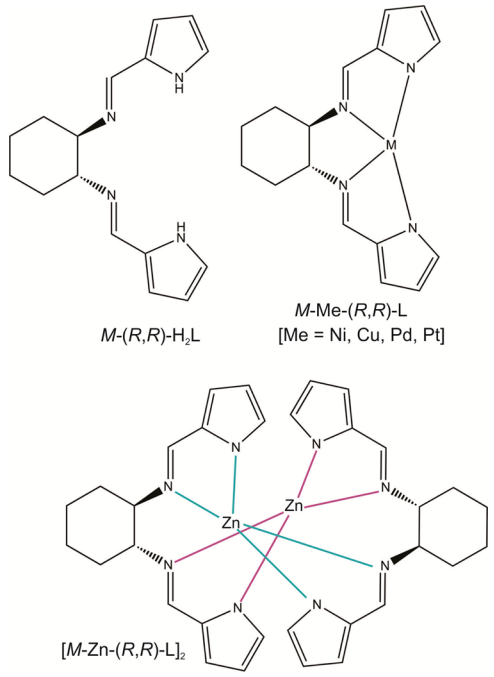

Figure 1. *M*-(*R*,*R*)-H_2L ligand and its transition metal complexes, namely, *M*-Ni-(*R*,*R*)-L, *M*-Cu-(*R*,*R*)-L, *M*-Pd-(*R*,*R*)-L, *M*-Pt-(*R*,*R*)-L, and [*M*-Zn-(*R*,*R*)-L]$_2$ studied here. Both the (*R*,*R*) and (*S*,*S*) enantiomers of the ligands and complexes were synthesized.

pyrrole ring, and the H_{py} atom is intramolecularly hydrogen (H)-bonded with the nitrogen atom of the −N═C group. In H_2L, the cyclohexane ring takes on the chair configuration, as this is by far the dominant arrangement versus the boat configuration at room temperature.[27] The nitrogen atoms at the cyclohexane ring may both adopt either equatorial (equ) or both axial (ax) positions imposed by its (*R*,*R*) configuration (see Figure 2). Furthermore, these N atoms may take on either cis or trans orientations with respect to the nitrogen atoms of the pyrrole rings. A definition of the cis arrangement and the rotatable bonds is provided in Figure 2. The initial conformational search using the HF/STO-3G methods implemented in the Spartan package[28] produced seven candidates. These preliminary conformers were reoptimized at the B3LYP/cc-

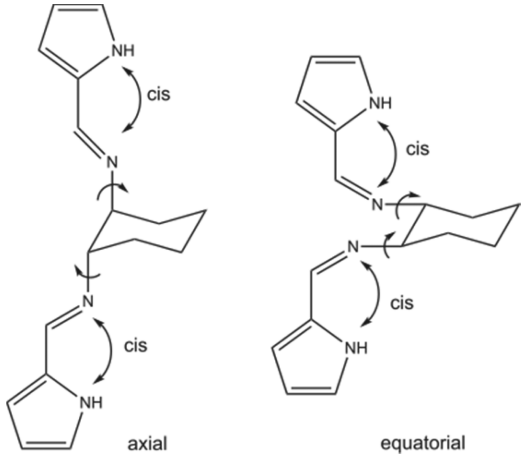

Figure 2. Cis configuration of (*R*,*R*)-H_2L ligand with axial and equatorial arrangement at cyclohexane. The rotatable N−C_{hexane} bonds are indicated by small arrows.

DOI: 10.1021/acs.inorgchem.5b00386
Inorg. Chem. 2015, 54, 4539−4549

pVTZ level of theory, and the four most stable conformers are given in Figure 3. The relative energies of these conformers

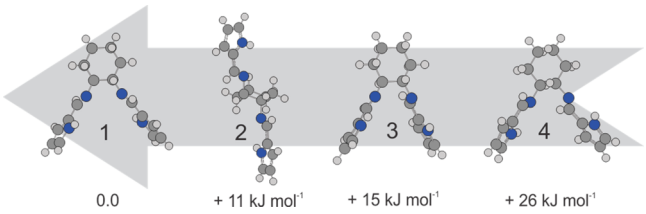

Figure 3. Relative free energies and geometries of the four most stable conformers of H_2L obtained at the B3LYP/cc-pVTZ level of theory in DMSO.

indicate that the equatorial cis−cis conformer, that is, $[cis-cis]_{equ}$ (Figure 2), is by far the dominant species at room temperature. Contributions from other conformers are negligible. It is noted that H_2L and other related ligands studied before all favor the equatorial arrangement. It is also not surprising that the cis−cis configuration is preferred since this arrangement enables the intramolecular H-bonding interaction between −NH of the pyrrole group and the nitrogen atom of the −C═N group. The resonance structure between the two aforementioned groups bestows structural rigidity to the ligand.

Figure 4 shows the experimental and calculated IR and VCD spectra obtained for the (*R*,*R*)-H_2L ligand in deuterated dimethyl sulfoxide (DMSO-d_6). Comparison of the experimental and calculated spectra reveal that conformer 1 is by far the dominant species in solution, consistent with the prediction by the relative energies. In ref 21, two main ligand conformations were suggested: one corresponding to conformer 1 and the other to conformer 4. Conformer 4 has negligible contribution in solution based on its relative free energy (Figure 3), and this conclusion is further supported by the comparison of the experimental and theoretical VCD spectra provided in Figure 4, where conformer 4 clearly makes little contribution to the experimental VCD spectral features. Note that we chose not to scale the frequency axis for straightforward discussion later on for vibrational frequency shift upon complexation. As one can see, the calculated VCD spectrum of conformer 1 captured all major experimental spectral features. The bands in the 1650−1600 cm^{-1} region correspond to both the in-phase and out-of-phase −C═N stretching modes. In the range below 1600 cm^{-1}, the vibrational modes can be assigned mainly to −C−H and −N−H bending motions of the pyrrole ring and different −CH and $-CH_2$ vibrational modes of the cyclohexane ring. The vibrational mode analysis of the ligand molecule in this region is provided in Figure S1, Supporting Information.

Figure 5 provides the experimental UV−vis and ECD spectra of the ligand and the related calculated spectra obtained for conformer 1 of the (*R*,*R*)-H_2L ligand in acetonitrile. The dominant negative Cotton couplet in the longer wavelength region was well-reproduced theoretically, as were the smaller features in the shorter nanometer region. Overall, a very good agreement between the experimental and calculated spectra was achieved, supporting the above conclusion that conformer 1 is the dominant species in solution. Note that we used a rather large number of electronic states of 200 to fully capture the band shape in the short wavelength region. Closer examination shows that in conformer 1, the two pyrrole subunits attached to the cyclohexane ring are held in a spatial arrangement that can be classified as *M* helicity. The dihedral angle θ, that is, the helicity-determining angle, between the plane N1−C2−C3−N4 and the corresponding plane N5−C6−C7−N8 (see Figure S2, Supporting Information for the atom labeling and detailed definition of the angle) in H_2L is 63.4°. Clearly, there is a severe deviation from a planar geometry for these two planes containing two N atoms each. It would be quite interesting to investigate how this helicity-determining angle θ changes upon coordination to different metals. Whether the helicity of the metal complexes is imposed by the ligand chirality and whether one can use VCD and/or ECD spectroscopy to determine if (*R*,*R*)-H_2L adopts *M* or *P* helicity in solution directly will be further explored in Section 2.4.

The previously reported H_2L crystal structure contains a water molecule, and its solid-state ECD spectrum shows noticeable differences from the solution spectrum.[21] More specifically, the solid-state ECD spectrum of (*R*,R)-H_2L contains two strong bisignate CD couplets at 250 and 310 nm, whereas the solution ECD measurement has just one positive Cotton couplet at 277 nm. The former was empirically

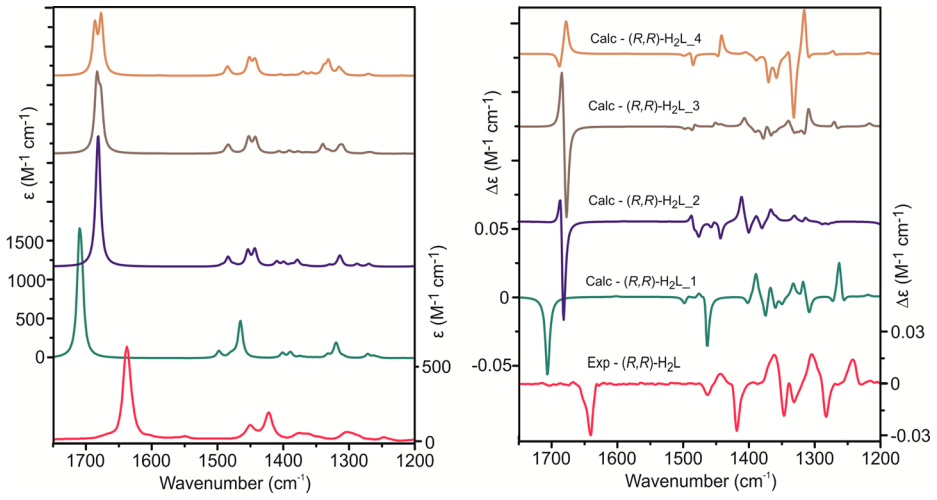

Figure 4. Comparison of the experimental IR (left) and VCD (right) spectra of the (*R*,*R*)-H_2L ligand in DMSO-d_6 with the corresponding theoretical spectra of the four H_2L conformers calculated at the B3LYP/cc-pVTZ level of theory in DMSO-d_6 solution.

DOI: 10.1021/acs.inorgchem.5b00386
Inorg. Chem. 2015, 54, 4539−4549

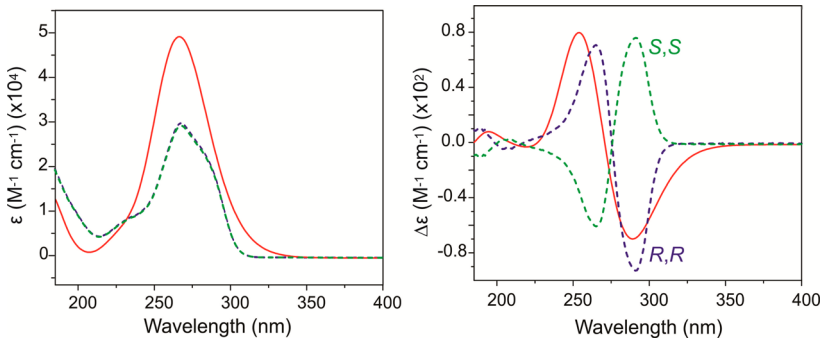

Figure 5. Comparison of the experimental (dashed) UV–vis (left) and ECD (right) spectra of (*R*,*R*)-H_2L (blue) and (*S*,*S*)-H_2L (green) in acetonitrile with the corresponding spectra (solid, red) of (*R*,*R*)-H_2L conformer 1 calculated at the B3LYP/cc-pVTZ level of theory in acetonitrile solution. 200 electronic states were included in the calculation.

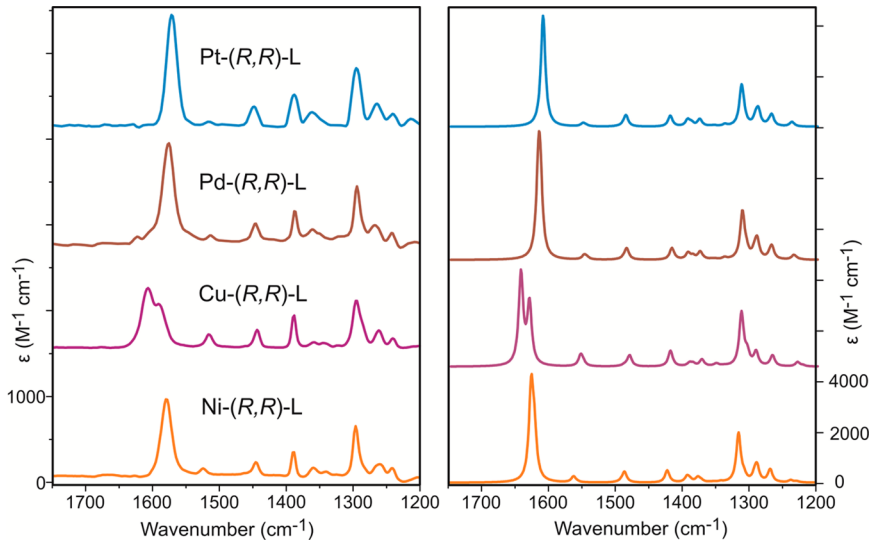

Figure 6. Comparison of the experimental IR spectra of the Ni(II), Cu(II), Pd(II), and Pt(II) complexes in DMSO-d_6 with the corresponding calculated spectra (right) at the B3LYP/Gen level of theory in DMSO-d_6 solution.

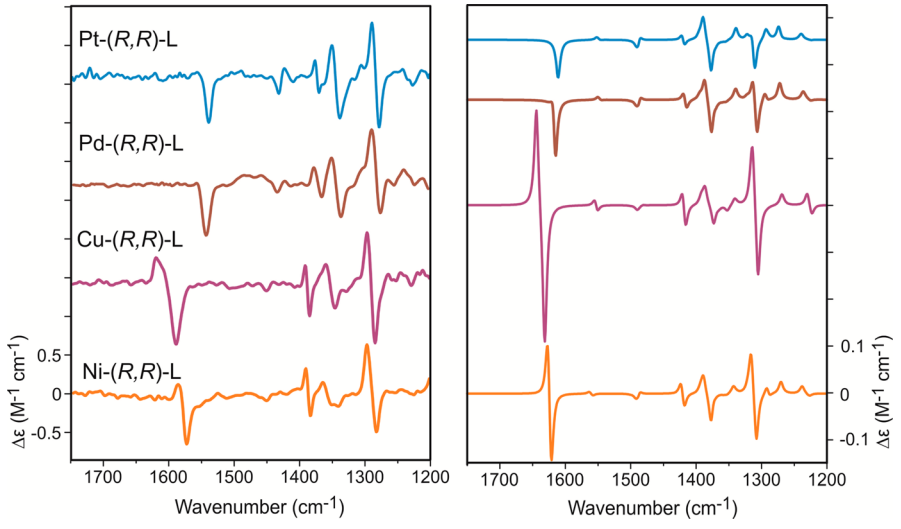

Figure 7. Comparison of the experimental VCD spectra of the Ni(II), Cu(II), Pd(II), and Pt(II) complexes in DMSO-d_6 with the corresponding calculated spectra (right) at the B3LYP/Gen level of theory in DMSO-d_6 solution.

ascribed to a pair of intermolecular exciton chromophores in the two H_2L molecules linked by a water molecule.[21] In a number of recent studies, the computational approach, which is based on the evaluation of two-body effects between the closest neighbors found in organic crystals, has been applied successfully to reproduce the solid-state CD spectra of organic molecules, in the presence of weak, moderate, and strong intermolecular interactions in the crystals.[29] We therefore

DOI: 10.1021/acs.inorgchem.5b00386
Inorg. Chem. 2015, 54, 4539–4549

constructed five model systems to examine the causes for the differences in solution and solid ECD spectra. These are H_2L [optimized] and H_2L-water [optimized] where both geometries were optimized in the gas phase, and H_2L-water [crystal], H_2L-water-H_2L [crystal], and water-H_2L-water-H_2L-water [crystal] where the crystal structural parameters were used without further optimization. The resulting theoretical UV−vis and ECD spectra are summarized in Figure S3, Supporting Information. Overall, all the UV−vis and ECD spectra look quite similar, excepting some minor changes in the short wavelength region below 200 nm. The intensity for H_2L-water-H_2L[crystal] and water-H_2L-water-H_2L-water [crystal] is higher, simply because there are two H_2L molecules in each system. Both H_2L-water-H_2L [crystal] and water-H_2L-water-H_2L-water [crystal] systems can be regarded as models for the proposed intermolecular exciton chromophores in solid. However, only one positive Cotton couplet was predicted for H_2L-water-H_2L[crystal] and water-H_2L-water-H_2L-water [crystal] in the region of interest with a slight red shift compared to that for H_2L by itself. The above results indicate that the intermolecular interactions in the crystal are likely *not* the only source for the noticeable differences observed in solid and in solution, and other factors in solid, which have not been considered in these models, are important. The above discussion also highlights the challenge in reproducing chiroptical response or even just structures in solid state,[30] and further extensive modeling is out of the scope of the current study.

2.2. Experimental and Theoretical IR and VCD spectra of the Ni(II), Cu(II), Pd(II), and Pt(II) Complexes. The experimental IR and VCD spectra for the Ni(II), Cu(II), Pd(II), and Pt(II) complexes are provided in Figures 6 and 7, respectively. As one can see, IR spectra are similar among the four complexes and the same vibrational assignment for the ligand holds for the metal complexes, with two exceptions. First, the spectrum for the Cu(II) complex shows an additional shoulder for the −C═N stretching vibrational mode, indicating a larger separation of the in-phase and out-of-phase −C═N stretching modes. Second, each complex displays an overlapped band in the 1525−1500 cm^{-1} region, due to the overlap of the in-phase and out-of-phase asymmetric C═C═C stretching modes which have essentially no intensity for the corresponding ligand discussed above. Detailed assignments of these vibrational modes are illustrated in Figure S4, Supporting Information, using the Cu(II) complex as an example. Similarly, VCD spectral features also resemble each other in the region below 1500 cm^{-1}. The most prominent difference among them for the VCD features is that the Ni(II) and Cu(II) complexes produce a bisignate +/- signal from low to high frequencies around 1600 cm^{-1}, whereas a negative band is observed for the Pd(II) and Pt(II) complexes instead.

To interpret the observed IR and VCD spectra of the complexes, theoretical conformational and configurational searches were performed for these four complexes with (*R*,*R*)-H_2L. All four metal complexes feature one dominant structure with a nearly square-planar coordination geometry (Figure 8), consistent with the X-ray crystal structures reported.[21,24,25] In these mononuclear complexes, the diamagnetic Ni(II), Pd(II), and Pt(II) ions take on a d^8 electron configuration with $3d_{z^2}$ orbital as the HOMO, while the paramagnetic Cu complex takes on a d^9 electron configuration with $3d_{x^2-y^2}$ orbital as the HOMO. Therefore, for the Ni, Pd, and Pt metal centers, $3d_{x^2-y^2}$ orbital is the LUMO, whereas for Cu, $4d_{yz}$ is the LUMO since all its 3d orbitals are either full or

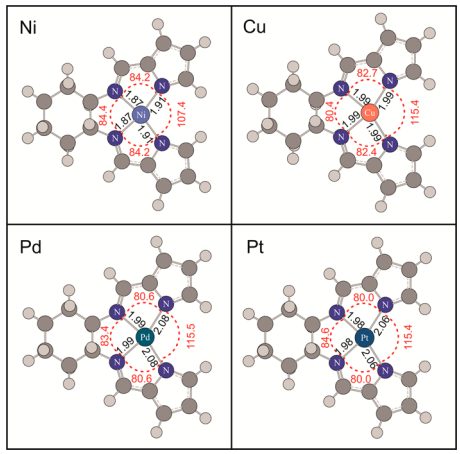

Figure 8. Most stable diastereomeric conformer of the mononuclear Cu(II), Ni(II), Pd(II) and Pt(II) complexes predicted at the B3LYP/Gen level of theory. The coordination bond distances (black, in Å) and angles (red, in deg) are also listed.

half-full and $4d_{yz}$ is the next lowest energy d orbital available. For the metal-N bonds, the N atom of the −C═N group shares its lone pair electrons through a dative-covalent bond using a sp^2-hybridized orbital in the *xy* plane, while the metal center utilizes a sp^2d hybrid orbital and therefore takes on a square-planar coordination geometry. The hybridization picture discussed here and the corresponding molecular orbital representations of the Cu and Ni complexes are provided in Figure S5, Supporting Information.

The simulated IR spectra (Figure 6) provide good agreements with the experiment. For the IR peaks below 1500 cm^{-1}, there are only very minor differences among these four metal complexes, indicating that the metal center has little effect on the vibrational modes of the pyrrole subunits and the cyclohexane rings. For the −C═N stretching vibrational modes near 1620 cm^{-1}, noticeable vibrational frequency shifts were predicted among these four metal complexes, reproducing the experimental shifts. Such shifts can be understood by examining the electronegativity of the metal centers, which act as Lewis acids with the following order: Cu(II) < Ni(II) < Pd(II) < Pt(II). Since the metal center pulls away electron density at the −C═N group (Lewis base), these −C═N bonds become weaker. One therefore expects that a larger electronegativity results in a larger red shift of the related −C═N stretching mode. Such a shift can also be viewed qualitatively from the hybridization picture in Supporting Information, Figure S5 where the metal−N σ bond can achieve a better head-to-head overlapping with a $sp^2d_{x^2-y^2}$ hybrid orbital in the case of Ni, Pd, and Pt than with a sp^2d_{yz} hybrid orbital of Cu. The weaker Cu−N bond results in higher −C═N stretching frequency for Cu than Ni. Overall, the trend observed experimentally follows the prediction: ligand (1640 cm^{-1}) > Cu (1610 cm^{-1} and 1593 cm^{-1}) > Ni (1580 cm^{-1}) > Pd (1578 cm^{-1}) > Pt (1572 cm^{-1}).

Similarly, the observed VCD spectral features for all four metal complexes are well-captured by the simulated ones (Figure 7). It is interesting to examine the cause of the significant VCD spectral variation in the −C═N stretching region around 1620 cm^{-1}. In particular, the Cu complex seems to show some sort of VCD intensity enhancement. The calculated VCD and IR intensities and their ratios for the −C═N stretching bands are tabulated in Table S1, Supporting

DOI: 10.1021/acs.inorgchem.5b00386
Inorg. Chem. 2015, 54, 4539−4549

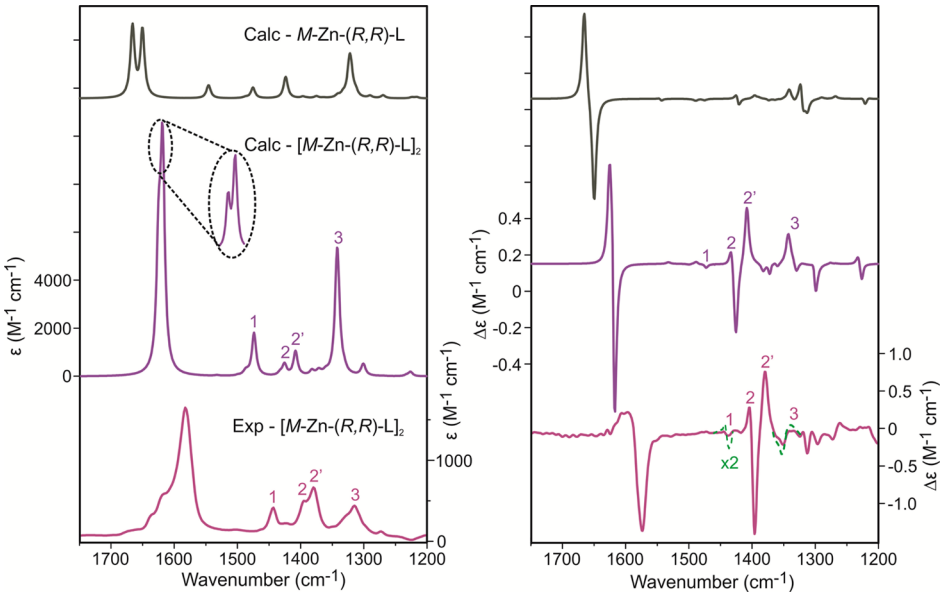

Figure 9. Comparison of the experimental IR (left) and VCD (right) spectra of the Zn(II) complex in DMSO-d_6 with the corresponding spectra of the mono- and dinuclear Zn(II) complexes calculated at the B3LYP/Gen level of theory in DMSO-d_6 solution. The dotted line marked with "x2" in the VCD spectra indicates that the intensity in the region is amplified by a factor of 2.

Information. A closer examination shows that the R/D ratios, where *D* is the dipole strength and *R* is the rotational strength for the Cu complex are nearly the same as for Ni and similar to those for Pt and Pd. The appearance of the enhancement is actually because the −C═N in-phase (mode 93) and out-of-phase vibrational (mode 92) modes for Cu are the most separated among the four, followed by Ni, Pd, and Pt. Since these two modes have opposite VCD signs, this results in a *single* negative VCD band for Pd and Pt where modes 92 and 93 are *nearly* on top of each other. For Ni, the VCD intensity of the two modes partially cancels each other, resulting in a lower intensity bisignate VCD feature. For Cu, such cancellation is the mildest, resulting in a relatively strong bisignate VCD feature.

Although the most stable coordination structures for all four metal complexes in solution were derived to be of nearly square-planar geometry, there is still subtle deviation from planarity, and all of them adopt *M* helicity. One may wonder what are the factors favoring this *M*-preference and if there might be substantial *P* helicity in solution as well. This topic will be further examined in Section 2.4. We also note that DMSO may potentially coordinate to the metal complexes. For example, two DMSO molecules were reported to coordinate to Ni(II) in the cis-arrangement in a Ni(II) complex with (*R*)-2,2′-bis(salicylideneamino)-1,1′-binaphthyl ligand and cause a noticeable twist of the Schiff-base backbone, resulting in changes in the VCD spectral features.[6] As mentioned before, the observed VCD spectral features of all the above metal complexes can be well-explained by the nearly square-planar coordination with H_2L, and therefore no further coordination with DMSO is explored here.

2.3. Experimental and Theoretical IR and VCD Spectra of the Zn(II) Complex. Experimental IR and VCD spectra of the Zn(II) complex are provided in Figure 9. One immediately obvious observation is that both IR and VCD spectra of the Zn(II) complex differ noticeably from those of the four metal complexes discussed above. In particular, Zn shows a strong trisignate VCD couplet in the 1400 cm^{-1} region that is not observed in any others. Since all d orbitals are fully occupied and Zn(II) takes on the singlet A state here, the Zn(II) ion takes on sp^3 hybridization to make covalent bonds with the p orbitals (sp^2 hybridization) of the nitrogen atoms of the −C═N groups, favoring the tetrahedral coordination configuration about the metal center. Indeed, the optimized geometry of the mononuclear Zn(II) complex deviates considerably from a perfect square-planar arrangement, in comparison to the four metal complexes discussed above. The corresponding simulated IR and VCD spectra of the mononuclear Zn(II) complex are given in Figure 9. In contrast to the situation with the other four mononuclear complexes, the simulated IR and especially VCD spectra of the mononuclear Zn(II) complex show poor agreement with the experimental data.

Therefore, we explored the possible formation of a dinuclear Zn(II) complex in solution. In such a complex, the two Zn(II) metal centers both adopt a nearly tetrahedral coordination geometry to form a double-stranded dinuclear helix (Figure 1), as illustrated previously by X-ray crystallography.[21] The geometry of the dinuclear Zn(II) complex was optimized in solution. The simulated IR and VCD spectra are given in Figure 9. In the 1700−1550 cm^{-1} region, both the mono- and dinuclear complexes show slightly split vibrational bands and similar bisignate VCD signals. These calculated spectral features agree reasonably well with the experimental results in both cases. In addition, the dinuclear complex actually contains four distinctive −C═N stretching modes (see Figure S6, Supporting Information) in this region where the symmetric and antisymmetric stretching modes are grouped together at lower and higher frequencies, respectively.

In the 1550−1200 cm^{-1} region, the experimental spectrum is composed of four peaks visually, marked with 1, 2, 2′, and 3. General assignments of the calculated IR modes of the mono- and dinuclear Zn(II) complexes are summarized in Figure S7, Supporting Information. The IR band associated with the C═C═C stretching mode shows noticeably at ∼1550 cm^{-1} for the mononuclear complex but has almost no intensity for the dinuclear complex. The latter is consistent with the

DOI: 10.1021/acs.inorgchem.5b00386
Inorg. Chem. 2015, 54, 4539−4549

experimental observation. Furthermore, the predicted spacing among the IR bands in the 1500−1350 cm^{-1} region differs greatly for the two complexes, with the dinuclear one showing much better agreement with the experiment. At the same time, the predicted VCD spectral patterns of the mono- and dinuclear complexes also differ greatly, especially in the region around 1400 cm^{-1}. The strong +/-/+ features observed in this region match those of the dinuclear complex only. Therefore, the comparison of the experimental and theoretical IR and VCD spectra allows one to confidently identify the dinuclear Zn(II) complex as the dominant species in solution. This demonstrates the utility of VCD spectroscopy as a powerful tool to illustrate detailed structural features of chiral species directly in solution.

2.4. *M* and *P* Helicity in the Metal Complexes and the Ligand. The theoretical and experimental results discussed above show that the (*R*,*R*)-H_2L ligand and the associated transition metal complexes all take on *M* helicity. In this section, we first examine the cause for such specific helicity preference. For the metal complexes, the helicity-determining angle θ, following the notation used in ref 4, is defined as the dihedral angle between the N1-Metal-N2 and the N3-Metal-N4 planes in Figure 10a, where N1 and N2 belong to one pyrrole arm, and N3 and N4 belong to the other arm. These angle values are compared in Table 1 for all species studied in solution and in crystal form, while their structures in solution and in solid are compared in Figure S8, Supporting Information. For example, the θ value for the H_2L ligand by itself is 63.4° and 64.4° with water, in comparison to 70.5° obtained from the solid-state structure, which contains crystal water.[21] It appears that the ligand structure remains much the same, regardless of the coordination to water or the lattice forces and other environmental perturbation in solid state. In addition, the θ values for the ligand and for the dinuclear Zn(II) complexes are similar. Indeed, the formation of the dinuclear Zn(II) complex offers an efficient way to allow the Zn(II) center to follow its tetrahedral coordination tendency, without putting much strain on the cyclohexane rings. A detailed examination shows that the rigidity of the cyclohexane ring in the preferred chair configuration and the (*R*,*R*) configuration of the ligand dictates that the ligand takes on *M* helicity. The *P*-(*R*,*R*) diastereomer could only be generated with the cyclohexane ring in a boat configuration (vide infra), which is known to have negligible population at room temperature.[31]

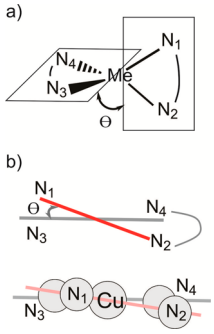

Figure 10. (a) Definition of the helicity-determining angle θ. For tetrahedral, θ = 90°, whereas for square planar, θ = 0°. N_1 and N_2 are atoms of one pyrrole arm, and N_3 and N_4 are atoms of the other arm. (b) Illustration of the *M* helicity in the nearly square planar metal complexes with the (*R*,*R*) ligand, viewing the coordination arraignment in (a) from the right side. Note that N_2 and N_4 are connected by the cyclohexane ring. The calculated structure of the Cu complex in solution with the (*R*,*R*) ligand is used as an example at the bottom. Note that all other atoms are removed for clarity.

Table 1. Helicity-Determining Angle θ for the H_2L Ligand and the Associated Complexes

compound	θ (deg) solution[a]	θ (deg) solid[b]
M-Pt-(*R*,*R*)-L	3.3	6.7
M-Pd-(*R R*)-L	3.7	7.5
M-Ni-(*R R*)-L	5.2	6.5
M-Cu-(*R R*)-L	8.5	18.5
M-Zn-(*R*,*R*)-L[c]	26.5	
(*M*-Zn-(*R*,*R*)-L)$_2$	75.9	80.9
M-(*R*,*R*)-H_2L	63.4[d]	70.5[d,e]
(*M*-Zn-(*R*,*R*)-L)$_2$	74.4[f]	78.3[f]

[a]These are based on the optimized geometries in the respective solvents. [b]These are based on the X-ray structural parameters reported in refs 20, 21, 24, and 25. [c]Calculated hypothetical mononuclear Zn-(*R*,*R*)-L compound in DMSO. [d]This is the dihedral angle defined in Figure S2, Supporting Information. [e]Note the crystal structure of the ligand contains water. See ref 21 for details. [f]This is the dihedral angle between the N1−Zn−N2 and N7−Zn−N8 planes (see Figure 11 for atom labeling).

The other four metals, Pt(II), Pd(II), Ni(II), and Cu(II), on the other hand, favor a nearly square-planar coordination geometry. Coordination of the ligand with these metal centers serves to reduce the helicity angle close to zero. One may speculate that the *M* and *P* helicity may be interconverted in solution by a ligand rearrangement through a planar coordination geometry since these four complexes are only slightly distorted from a square-planar geometry. Considerable efforts were spent to generate both *M*-(*R*,*R*) and *P*-(*R*,*R*) diastereomers. It became clear that the strong preference of the cyclohexane ring in chair configuration and the (*R*,*R*) configuration again impose that the complexes adopt the *M* helicity. Even though all these complexes are in nearly square-planar coordination geometry, only one dominant diastereomeric structure, namely, *M*-(*R*,*R*), is identified for each in solution, as shown in Figure 8. Figure 10b shows the helicity of these nearly planar complexes using the Cu complex as an example.

While *M* helicity of the diamine ligand appears to be preserved in all the subsequent metal complexes in the current study, induced helicity in the (*R*,*R*)-*N*,*N*′-bis(5-*tert*-butylsalicylidene)-1,2-cyclohexanediamine (salen)−metal complexes with chiral diamine ligands exhibits some fascinating diversity. When Fox and co-workers juxtaposed different elements of chirality that are predisposed to folding in several chiral nickel-salen complexes, they found that *trans*-cyclohexane-1,2-diamine is a weak director of absolute helicity in these complexes and that the helicity of the complexes was more strongly influenced by the end-group chirality than the central chirality.[32] We note that, while *trans*-cyclohexane-1,2-diamine is shown to dictate the helicity of the resulting metal complexes in the present study, its square-planar metal complexes possess only subtle helicity themselves. It is perhaps not surprising that the aforementioned salen-Ni complexes, which were arranged in similar nearly square-planar coordination geometries, exhibit weak ability to direct the folding of the substituted arms. In addition, it is not just the central chirality of the ligand but also the strong chair preference of the cyclohexane ring that direct the helicity of the metal-complexes studied here.

DOI: 10.1021/acs.inorgchem.5b00386
Inorg. Chem. 2015, 54, 4539−4549

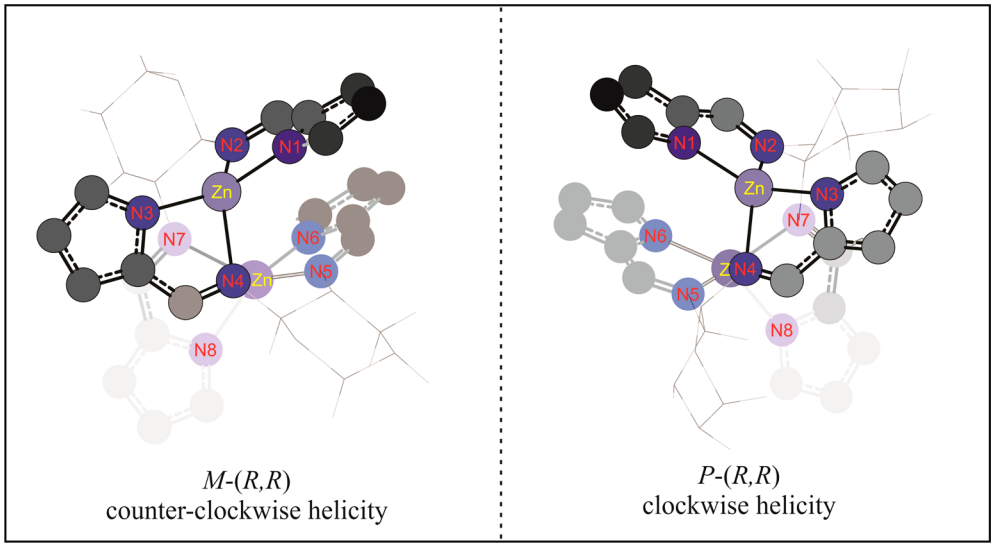

Figure 11. Illustration of the *M* and *P* helicity for the dinuclear Zn(II) complex.

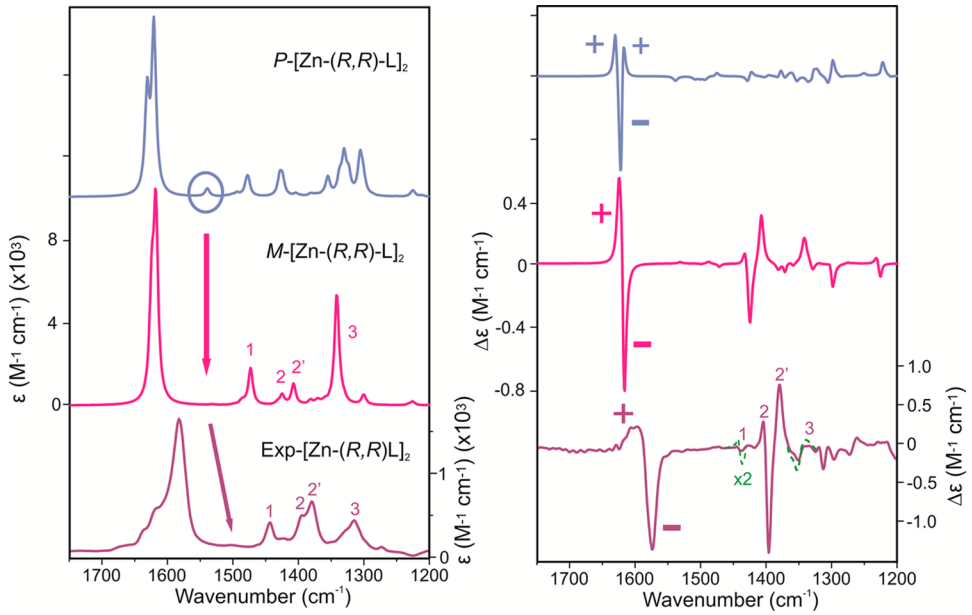

Figure 12. Comparison of the experimental IR (left) and VCD (right) spectra of the Zn(II) complex in DMSO-d_6 with the corresponding spectra of the *M*- and *P*-[Zn-(*R*,*R*)-L]$_2$ diastereomers calculated at the B3LYP/Gen level of theory in DMSO-d_6 solution. The dotted line marked with "x2" in the VCD spectra indicates that the intensity in the region is amplified by a factor of 2.

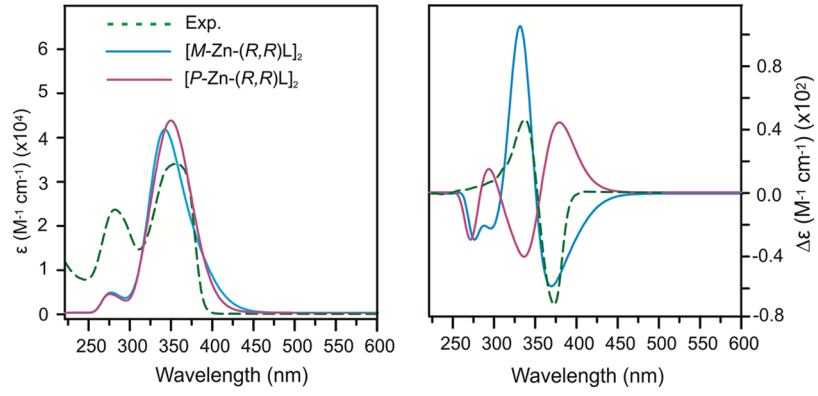

Figure 13. Comparison of the experimental UV–vis (left) and ECD (right) spectra of the Zn(II) complex in acetonitrile with the corresponding spectra of the *M*- and *P*-[Zn-(*R*,*R*)-L]$_2$ diastereomers calculated at the B3LYP/Gen level of theory in acetonitrile solution.

DOI: 10.1021/acs.inorgchem.5b00386
Inorg. Chem. 2015, 54, 4539–4549

Next, we evaluate if VCD or ECD spectral features themselves are sufficient to tell apart *M*-(*R*,*R*) and *P*-(*R*,*R*) diastereomers, in other words, if VCD or ECD spectral features are sensitive to both ligand chirality and *M* (or *P*) helicity of the molecule. We use the Zn(II) complex as an example. Two diastereomeric geometries of the dinuclear Zn(II) complex were optimized and are provided in Figure 11, where the *P*-configuration is ∼60 kJ/mol less stable.

Figure 12 shows the comparison of the experimental and theoretical IR and VCD spectra of the *M*- and *P*-[Zn-(*R*,*R*)-L]$_2$ structures. There are a number of significant differences between the IR and VCD spectra of the *P* and *M* helical structures. For example, the experimental IR spectrum below 1500 cm^{-1} is comprised of four distinctive intense signals. This observation is only reproduced by the *M* helical structure. Furthermore, the -/+ bisignate VCD features (from low to high cm^{-1}) in the 1650−1550 cm^{-1} region were only captured with the *M* configuration and not at all by the *P* configuration. Lastly, for the region between 1450 and 1350 cm^{-1}, there exists an obvious +/-/+ couplet that can be only observed for the *M* configuration, while it is missing for the other one. Therefore, one can conclude confidently that *M*-[Zn-(*R*,*R*)-L]$_2$ is by far the dominant species in solution based on the IR and VCD spectral feature comparison alone.

We further investigate the differences in the UV−vis and especially ECD spectra for the *M*- and *P*-Zn(II) complex. In Figure 13, we show the comparison of the experimental and theoretical UV−vis and ECD spectra of the *M*- and *P*-[Zn-(*R*,*R*)-L]$_2$ diastereomers. As one can see, the predicted UV−vis spectra for the *M*- and *P*-Zn(II) diastereomers are very similar. The corresponding ECD spectra, on the other hand, show essentially the mirror-imaged spectral features in most parts, except at ∼275 nm where a negative band was predicted for both. It appears that the ECD features are dominated by the helicity of the compound, while the feature at 275 nm reflects the ligand chirality. As one can see clearly from Figure 13, the experimental ECD spectrum observed is only consistent with the *M*-[Zn-(*R*,*R*)-L]$_2$ diastereomer, supporting the conclusion drawn from the IR and VCD study.

It is important to emphasize that VCD spectra of *M*-[Zn-(*R*,*R*)-L]$_2$ and *P*-[Zn-(*R*,*R*)-L]$_2$ do not show nearly mirror-image quality to each other as in the case of ECD. Rather, they exhibit sensitivity to both ligand chirality and the helicity of the complex. In addition, IR spectra for these two diastereomers are also quite different, whereas their UV−vis spectra are very much alike. Therefore, one cannot tell *M*-[Zn-(*R*,*R*)-L]$_2$ apart from *M*-[Zn-(*S*,*S*)-L]$_2$ based on the UV−vis and ECD spectra of the sample alone, whereas IR and VCD spectra allow us to identify them unambiguously.

While *M*- and *P*-[Zn-(*R*,*R*)-L]$_2$ exhibit nearly mirror-imaged ECD spectra, the *M*- and *P*-diastereomers of the di-μ-oxo dimanganese(IV) complex with tetradentate salen ligands were reported to have very similar ECD spectra.[12] In addition, in the same study, the di-μ-oxo dimanganese(IV) complex was shown to afford a mixture of *M*-(*R*,*R*) and *P*-(*R*,*R*) diastereomers. These apparent contradictions merit some explanations. First, one would expect the salen ligands with the cyclohexane rings to exert a similar constraint on the helicity of the mononuclear units, and this appeared to be the case. The overall helicity of the dimanganese complex, on the other hand, is induced by the relative twist of the top and bottom mononuclear units about the metal−metal axis. The sense of the twist, that is, *M* or *P*, is strongly influenced by the tetradentate salen ligands bearing different degrees of steric bulk and by the center metals, for example, Mn versus Ti. Second, the dimanganese ECD spectra are dominated by the response from the mononuclear units, whereas the aforementioned twist only slightly modifies the ECD spectrum of the dimanganese complex.[12] This discussion highlights the complexity one may encounter in interpreting the observed ECD spectrum and the significant advantages in using multiple chiroptical techniques and theoretical modeling to verify the explanation.[33]

While the experimental UV−vis and ECD spectra of the metal complexes were reported in several solvents before,[20,21,24,25] no theoretical calculations have been reported so far. For completion and easy comparison, we performed measurements for all five metal complexes in the same acetonitrile solvent and also the UV−vis and ECD calculations of the dominant species identified in solution. The comparisons of the experimental and theoretical data for all five metal complexes are summarized in Figure 14. As one can see, the

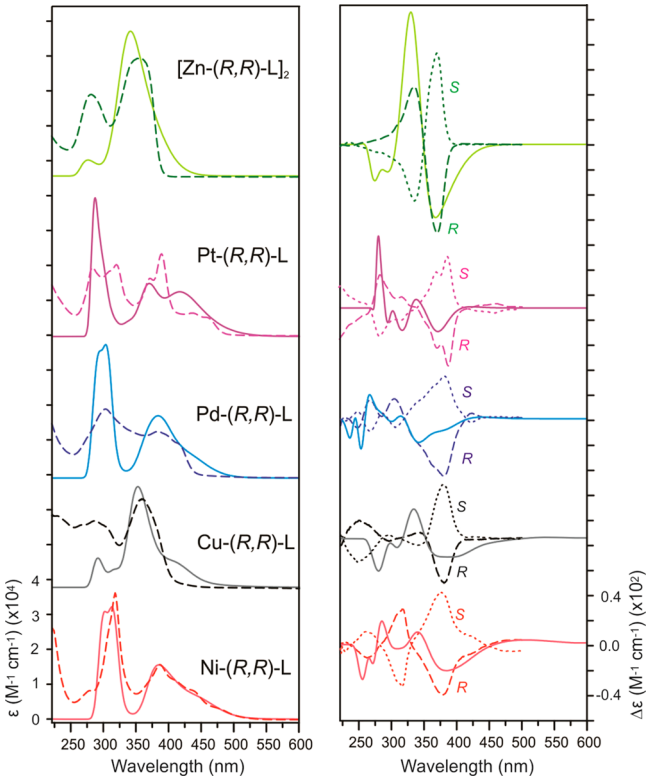

Figure 14. Comparison of the experimental (dotted and dashed) UV−vis and ECD spectra of the metal complexes in acetonitrile with simulated (solid) spectra of the *M*-(*R*,*R*) metal complexes at the B3LYP/Gen level of theory in acetonitrile solution. The first 100 electronic excited states were used in the spectral calculations. *R* and *S* indicate the ligand chirality of (*R*,*R*) and (*S*,*S*), respectively.

experimental ECD spectra of the five metal complexes with (*R*,*R*) ligand(s) *all* exhibit a negative Cotton couplet, which is well-reproduced by the theoretical modeling in all five cases. It is of no surprise that they exhibit the same negative Cotton couplet since the ECD spectral features are dominated by helicity of the system, that is, *M* helicity. Overall, the ECD investigation supports the conclusion derived from the VCD study. The agreement between experiment and theory deteriorates in the short wavelength region. In an effort to better capture the band shape in the short wavelength region,

DOI: 10.1021/acs.inorgchem.5b00386
Inorg. Chem. 2015, 54, 4539−4549

we further increased the number of electronic states computed with time dependent (TD)-DFT from 100 to 250. The results for the four metal complexes with 250 states are provided in Figure S9, Supporting Information. The improvement is only marginal. In addition, we also tested a recently developed and improved local approximation to the exchange−correlation density functional, MN12L,[34] for the UV−vis and ECD simulation. The results for Pt(II), Cu(II), and Ni(II) with 200 states are provided in Figure S10, Supporting Information. Visually, this functional provides better agreement with the experimental data. It would be worthwhile to explore the utility of this newer functional for other transition metal complexes in future studies.

3. EXPERIMENTAL SECTION

3.1. Synthesis. The yellow crystalline (*S*,*S*)-L and (*R*,*R*)-L molecules and both enantiomers of all transition metal complexes, Ni(II), Cu(II), Pd(II), Pt(II), and Zn(II), were synthesized and purified according to the reported synthetic procedures[21,24,25] using $Ni(ClO_4)_2{\cdot}6H_2O$, $Cu(ClO_4)_2{\cdot}6H_2O$, $Pd(OAc)_2$, K_2PtCl_4, and $Zn(OAc)_2{\cdot}2H_2O$ salts, respectively. The compounds were purchased from Sigma-Aldrich. The original literature ratios of reactants and solvents were used, while the number of moles of reactants and volume of solvents were scaled based on the desired amount of products, generally in the range from 25% to 110% of the reported amount in the original literature. Reaction times were tripled to ensure that reactions reached completion. Both the ligand and complexes are air-stable compounds. Both NMR and mass spectrometry analyses were performed, and the results were compared to the literature data to confirm the products obtained. These data are provided in Supporting Information.

3.2. Spectroscopic Measurements. IR and VCD spectra were measured using a Bruker Vertex 70 spectrometer with a PMA 50 module. The photoelastic modulator was set at 1400 cm^{-1} for all measurements. The signals were collected using a liquid nitrogen-cooled MCT detector for a period of 4 h (∼4300 scans) with 4 cm^{-1} resolution in the region of 1750−1200 cm^{-1}. DMSO-d_6 solutions of both enantiomers of the ligand and the nickel, copper, palladium, platinum, and zinc complexes with concentrations of 0.305, 0.015, 0.017, 0.011, 0.027, and 0.026 M, respectively, were prepared. These solutions were injected into a BaF_2 cell with a Teflon spacer of 0.1 mm for the ligand and 0.2 mm for the metal complexes. The reported IR spectra were background-corrected by subtraction of the solvent spectrum measured under identical condition. The reported VCD spectra were obtained by subtracting the VCD spectra of the two enantiomers and dividing by two. The UV−vis spectra of the prepared samples in acetonitrile were collected using an HP 8453 UV−vis instrument. The concentration and path length were optimized accordingly to have the UV−vis absorbance in the range of 0.2−0.9. The ECD spectra were recorded using an Olis DSM 17 CD spectrophotometer.

3.3. Theoretical Calculations. All conformational searches and geometric optimizations, spectral simulations, harmonic frequency calculations, and IR and VCD intensity predictions were performed by using the Gaussian 09 software packages.[35] The well-known B3LYP[36,37] hybrid functional was used for the DFT calculations.[38] The cc-pVTZ[39] basis set was used for the C, N, and H atoms and the LanL2DZ basis set for all the transition metals, namely, Ni(II), Cu(II), Pd(II), Pt(II), and Zn(II). To account for the bulk solvent environment, the integral equation formalism version of the polarization continuum model[40,41] using the universal force field radii was utilized. For this purpose, a dielectric constant of $\varepsilon = 46.826$ for DMSO was used. A Lorentzian line shape with a half-width at half-height (HWHH) of 4 cm^{-1} was used for the simulations of IR and VCD spectra. The UV−vis and ECD spectral simulations were performed by using the TD-DFT approach and by employing hybrid-GGA and Minnesota hybrid functional such as B3LYP and MN12L, respectively. All electronic optical spectra were simulated with the first 100 to 250 electronic excited states. To account for the solvent effect, a dielectric constant of $\varepsilon = 35.688$ was used for acetonitrile. A Gaussian line shape with an HWHH of 0.33 eV was used for the simulations of UV−vis and ECD spectra. The optimized coordinates for all the compounds studied are provided in Table S2, Supporting Information.

4. CONCLUSIONS

To gain insight into the relationship between the chiroptical spectral features and structural properties of transition metal complexes in solution, five transition metal, Ni(II), Cu(II), Pd(II), Pt(II), and Zn(II), complexes with the bis(pyrrol-2-ylmethyleneamine)-cyclohexane ligand were synthesized. Their structural properties, in particular, ligand chirality, helicity of the complexes, and coordination topology, have been explored in detail by using IR and VCD spectroscopy, as well as UV−vis and ECD spectroscopy, complemented with high-level DFT calculations. Comparison of the experimental and theoretical IR and VCD spectra allowed us to clearly identify the mononuclear Ni(II), Cu(II), Pd(II), and Pt(II) complexes and the dinuclear Zn(II) complex as the dominant species in their respective solutions. In addition to their coordination preference in solution, this study demonstrates that VCD spectroscopy offers the possibility to determine both the ligand chirality and the helicity of the ligand and the associated transition metal complexes. All systems investigated show *M* helicity with (*R*,*R*) ligand(s). This specific helicity preference is dictated by the conformation preference of the ligand, and its chirality and has little to do with the coordination topology or the associated metals. Theoretical simulations indicate that the experimental ECD spectra of the metal complexes, in contrast to VCD spectra, are dominated by the spectral features related to helicity. This is somewhat surprising, especially since four of the five metal complexes reported here adopt nearly square-planar coordination geometries whose helicity-determining angles are close to zero, and one may deem such helicity subtle. Comparison with the recently reported di-μ-oxo dimetal complexes points to the persistency of such subtle helicity and its dominant presence in the ECD spectra over the more obvious helicity induced by the twisting of the two mononuclear complex subunits about the metal−metal axis. We highlight the challenges in correctly interpreting the observed ECD spectra and the advantages in utilizing multiple chiroptical techniques and theoretical modeling in extracting detailed chiral information on metal complexes in solution.

■ ASSOCIATED CONTENT

Supporting Information

Selected IR spectra and spectral analyses, simulated UV−vis and ECD spectra of metal complexes, discussion of helicity-determining angle, ECD spectra, hybridized orbitals and molecular orbitals of complexes, calculated dipolar and rotational strengths, comparison of solid-state and solution structures, coordinates of optimized geometries. This material is available free of charge via the Internet at http://pubs.acs.org.

■ AUTHOR INFORMATION

Corresponding Author

*E-mail: yunjie.xu@ualberta.ca.

Author Contributions

The manuscript was written through contributions of all authors. All authors have given approval to the final version of the manuscript.

DOI: 10.1021/acs.inorgchem.5b00386
Inorg. Chem. 2015, 54, 4539−4549

Notes

The authors declare no competing financial interest.

■ ACKNOWLEDGMENTS

This research was funded by the University of Alberta and the Natural Sciences and Engineering Research Council of Canada. We gratefully acknowledge access to the computing facilities provided by the Shared Hierarchical Academic Research Computing Network (Sharcnet) and by the Western Canada Research Grid (Westgrid). Y.X. holds a senior Canada Research Chair in Chirality and Chirality Recognition.

■ REFERENCES

(1) Bellemin-Laponnaz, S.; Dagorne, S. *Chem. Rev.* **2014**, *114*, 8747−8774.
(2) Merten, C.; McDonald, R.; Xu, Y. *Inorg. Chem.* **2014**, *53*, 3177−3182.
(3) Wu, T.; Zhang, X.-P.; You, X.-Z.; Li, Y.-Z.; Bouř, P. *ChemPlusChem* **2014**, *79*, 698−707.
(4) Enamullah, M.; Uddin, A. K. M. R.; Pescitelli, G.; Berardozzi, R.; Makhloufi, G.; Vasylyeva, V.; Chamayou, A.-C.; Janiak, C. *Dalton Trans.* **2014**, *43*, 3313−3329.
(5) (a) Chamayou, A.-C.; Makhloufi, G.; Nafie, L. A.; Janiak, C.; Lüdeke, S. *Inorg. Chem.* **2015**, *54*, 2193−2203. (b) Chamayou, A.-C.; Lüdeke, S.; Brecht, V.; Freedman, T. B.; Nafie, L. A.; Janiak, C. *Inorg. Chem.* **2011**, *50*, 11363−11374.
(6) Sato, H.; Mori, Y.; Yamagishi, A. *Dalton Trans.* **2013**, *42*, 6873−6878.
(7) Wu, T.; You, X.; Bouř, P. *Coord. Chem. Rev.* **2015**, *284*, 1−18.
(8) Sato, H.; Yamagishi, A. *Int. J. Mol. Sci.* **2013**, *14*, 964−978.
(9) Magyarfalvi, G.; Tarczay, G.; Vass, E. *Wiley Interdiscip. Rev.: Comput. Mol. Sci.* **2011**, *1*, 403−425.
(10) Yang, G.; Xu, Y. In *Topics in Current Chemistry;* Naaman, R., Beratan, D. N., Waldeck, D. H., Eds.; Springer-Verlag: Berlin, Germany, 2011; Vol. *298*, pp 189−236.
(11) Dezhahang, Z.; Merten, C.; Poopari, M. R.; Xu, Y. *Dalton Trans.* **2012**, *41*, 10817−1082.
(12) Kurahashi, T.; Hada, M.; Fujii, H. *Inorg. Chem.* **2014**, *53*, 1070−1079.
(13) Merten, C.; Xu, Y. *Dalton Trans.* **2013**, *42*, 10572−10578.
(14) (a) Saito, M.; Sato, H.; Mori, Y.; Fukuda, Y. *Bull. Chem. Soc. Jpn.* **2009**, *82*, 1266−1273. (b) Telfer, S. G.; Kuroda, R. *Coord. Chem. Rev.* **2003**, *242*, 33−46.
(15) Sato, H.; Sato, F.; Taniguchic, M.; Yamagishi, A. *Dalton Trans.* **2012**, *41*, 1709−1712.
(16) Bacchi, A.; Carcelli, M.; Gabba, L.; Ianelli, S.; Pelagatti, P.; Pelizzi, G.; Rogolino, D. *Inorg. Chem. Acta.* **2003**, *342*, 229−235.
(17) Kano, S.; Nakano, H.; Kojima, M.; Baba, N.; Nakajima, K. *Inorg. Chem. Acta.* **2003**, *349*, 6−16.
(18) Nguyen, Q. T.; Jeong, J. H. *Polyhedron* **2006**, *25*, 1787−1890.
(19) Cristau, H.-J.; Ouali, A.; Spindler, J.-F.; Taillefer, M. *Chem.—Eur. J.* **2005**, *11*, 2483−2492.
(20) Shan, X. F.; Wu, L. Z.; Liu, X. Y.; Zhang, L. P.; Tung, C. H. *Eur. J. Inorg. Chem.* **2007**, 3315−3319.
(21) Wang, Y.; Fu, H.; Shen, F.; Sheng, X.; Peng, A.; Gu, Z.; Ma, H.; Ma, J. S.; Yao, J. *Inorg. Chem.* **2007**, *46*, 3548−3556.
(22) Eerdun, C.; Hisanaga, S.; Setsune, J. *Angew. Chem., Int. Ed.* **2013**, *52*, 929−932.
(23) Miyake, H. *Symmetry* **2014**, *6*, 880−895.
(24) Shan, X.-F.; Wang, D.-H.; Tung, C.-H.; Wu, L.-Z. *Tetrahedron.* **2008**, *65*, 5577−5582.
(25) Shan, X.-F.; Wang, D.-H.; Tung, C.-H.; Wu, L.-Z. *Chin. Sci. Bull.* **2007**, *52*, 1581−1584.
(26) Dezhahang, Z.; Poopari, M. R.; Xu, Y. *Chem.—Asian J.* **2013**, *8*, 1205−1212.
(27) Bachrach, S. M. *Computational Organic Chemistry;* John Wiley & Sons, Inc.: New York, 2007.
(28) Spartan 08 Wavefunction, Inc.; Irvine, C. A.; Shao, Y.; Molnar, L. F.; Jung, Y.; Kussmann, J.; Ochsenfeld, C.; Brown, S. T.; Gilbert, A. T. B.; Slipchenko, L. V.; Levchenko, S. V.; O'Neill, D. P.; DiStasio, R. A., Jr.; Lochan, R. C.; Wang, T.; Beran, G. J. O.; Besley, N. A.; Herbert, J. M.; Lin, C. Y.; Van Voorhis, T.; Chien, S. H.; Sodt, A.; Steele, R. P.; Rassolov, V. A.; Maslen, P. E.; Korambath, P. P.; Adamson, R. D.; Austin, B.; Baker, J.; Byrd, E. F. C.; Dachsel, H.; Doerksen, R. J.; Dreuw, A.; Dunietz, B. D.; Dutoi, A. D.; Furlani, T. R.; Gwaltney, S. R.; Heyden, A.; Hirata, S.; Hsu, C.-P.; Kedziora, G.; Khalliulin, R. Z.; Klunzinger, P.; Lee, A. M.; Lee, M. S.; Liang, W. Z.; Lotan, I.; Nair, N.; Peters, B.; Proynov, E. I.; Pieniazek, P. A.; Rhee, Y. M.; Ritchie, J.; Rosta, E.; Sherrill, C. D.; Simmonett, A. C.; Subotnik, J. E.; Woodcock, H. L., III; Zhang, W.; Bell, A. T.; Chakraborty, A. K.; Chipman, D. M.; Keil, F. J.; Warshel, A.; Hehre, W. J.; Schaefer, H. F.; Kong, J.; Krylov, A. I.; Gill, P. M. W.; Head-Gordon, M. *Phys. Chem. Chem. Phys.* **2006**, *8*, 3172−3191.
(29) (a) Pescitelli, G. *Chirality* **2012**, *24*, 718−724. (b) Pescitelli, G.; Padula, D.; Santoro, F. *Phys. Chem. Chem. Phys.* **2013**, *15*, 795−802. (c) Padula, D.; Pietro, S. D.; Capozzi, M. A. M.; Cardellicchio, C.; Pescitelli, G. *Chirality* **2014**, *26*, 462−470.
(30) Szalewicz, K. *Acc. Chem. Res.* **2014**, *47*, 3266−3274.
(31) Yang, G.; Tran, H.; Fan, E.; Shi, W.; Lowary, T. L.; Xu, Y. *Chirality* **2010**, *22*, 734−743.
(32) (a) Dong, Z.; Yap, G. P. A.; Fox, J. M. *J. Am. Chem. Soc.* **2007**, *129*, 11850−11853. (b) Dong, Z.; Bai, S.; Yap, G. P. A.; Fox, J. M. *Chem. Commun.* **2011**, *47*, 3781−3783.
(33) De Gussem, E.; Herrebout, W.; Specklin, S.; Meyer, C.; Cossy, J.; Bultinck, P. *Chem.—Eur. J.* **2014**, *20*, 17385−17394.
(34) Peverati, R.; Truhlar, D. G. *Phys. Chem. Chem. Phys.* **2012**, *14*, 13171−13174.
(35) Frisch, M. J.; Trucks, G. W.; Schlegel, H. B.; Scuseria, G. E.; Robb, M. A.; Cheeseman, J. R.; Scalmani, G.; Barone, V.; Mennucci, B.; Petersson, G. A.; Nakatsuji, H.; Caricato, M.; Li, X.; Hratchian, H. P.; Izmaylov, A. F.; Bloino, J.; Zheng, G.; Sonnenberg, J. L.; Hada, M.; Ehara, M.; Toyota, K.; Fukuda, R.; Hasegawa, J.; Ishida, M.; Nakajima, T.; Honda, Y.; Kitao, O.; Nakai, H.; Vreven, T.; Montgomery, J. A., Jr.; Peralta, J. E.; Ogliaro, F.; Bearpark, M.; Heyd, J. J.; Brothers, E.; Kudin, K. N.; Staroverov, V. N.; Kobayashi, R.; Normand, J.; Raghavachari, K.; Rendell, A.; Burant, J. C.; Iyengar, S. S.; Tomasi, J.; Cossi, M.; Rega, N.; Millam, N. J.; Klene, M.; Knox, J. E.; Cross, J. B.; Bakken, V.; Adamo, C.; Jaramillo, J.; Gomperts, R.; Stratmann, R. E.; Yazyev, O.; Austin, A. J.; Cammi, R.; Pomelli, C.; Ochterski, J. W.; Martin, R. L.; Morokuma, K.; Zakrzewski, V. G.; Voth, G. A.; Salvador, P.; Dannenberg, J. J.; Dapprich, S.; Daniels, A. D.; Farkas, Ö.; Foresman, J. B.; Ortiz, J. V.; Cioslowski, J.; Fox, D. J. *Gaussian 09,* Revision D.01; Gaussian, Inc.: Wallingford, CT, 2009.
(36) Becke, A. D. *J. Chem. Phys.* **1993**, *98*, 5648−5652.
(37) Lee, C. T.; Yang, W. T.; Parr, R. G. *Phys. Rev. B* **1988**, *37*, 785−789.
(38) Kohn, W.; Sham, L. J. *Phys. Rev.* **1965**, *140*, A1133−A1138.
(39) Kendall, R. A.; Dunning, T. H., Jr.; Harrison, R. J. *J. Chem. Phys.* **1992**, *96*, 6796−6806.
(40) Tomasi, J.; Mennucci, B.; Cammi, R. *Chem. Rev.* **2005**, *105*, 2999−3093.
(41) Mennucci, B.; Tomasi, J.; Cammi, R.; Cheeseman, J. R.; Frisch, M. J.; Devlin, F. J.; Gabriel, S.; Stephens, P. J. *J. Phys. Chem. A* **2002**, *106*, 6102−6113.

DOI: 10.1021/acs.inorgchem.5b00386
Inorg. Chem. 2015, 54, 4539−4549